

See discussions, stats, and author profiles for this publication at: <https://www.researchgate.net/publication/261740153>

# Favored Composition Design and Atomic Structure Characterization for Ternary Al-Cu-Y Metallic Glasses via Proposed Interatomic Potential

ARTICLE *in* THE JOURNAL OF PHYSICAL CHEMISTRY B · APRIL 2014

Impact Factor: 3.3 · DOI: 10.1021/jp502167t · Source: PubMed

---

CITATIONS

7

---

READS

21

4 AUTHORS, INCLUDING:



Qi Wang

Tsinghua University

11 PUBLICATIONS 19 CITATIONS

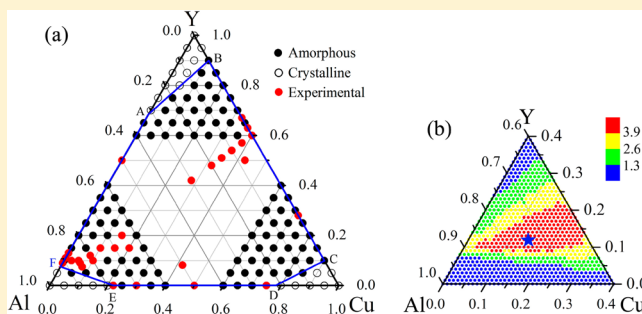
SEE PROFILE

# Favored Composition Design and Atomic Structure Characterization for Ternary Al–Cu–Y Metallic Glasses via Proposed Interatomic Potential

Q. Wang, J. H. Li, J. B. Liu, and B. X. Liu\*

Key Laboratory of Advanced Materials (MOE), School of Materials Science and Engineering Tsinghua University, Beijing 100084, China

**ABSTRACT:** A realistic interatomic potential is constructed for the Al–Cu–Y system under a newly proposed formalism and applied to perform atomistic simulations, leading to predicting a hexagonal composition region within which metallic glass formation is energetically favored and the region is defined as the *quantitative* glass formation ability of the system. Amorphization driving force of a glassy alloy is then calculated to correlate the readiness of its forming ability in practice, and a local optimized stoichiometry is pinpointed to be  $\text{Al}_{74}\text{Cu}_{14}\text{Y}_{12}$ , of which the metallic glass could be most stable or easiest obtainable. The predictions are well supported by the experimental observations reported so far in the literature. Further structural analysis indicates that adding Y extends the short-range landscape and facilitates developing a hybridized icosahedral- and fcc-like packing in the medium-range, eventually enhancing the glass formation ability of the system.



## I. INTRODUCTION

Ever since the discovery of melt-spun Al-based glassy ribbons in the 1980s, great effort has been made to pursue Al-based metallic glasses (MGs) in bulk form, in order to give full play to their unique properties, such as high specific strength and even good ductility. Recently, dramatic progress has been made in Al–TM–RE (TM, transition metal; RE, rare earth metal) alloy systems, and as a new family of bulk MGs, they have attracted plenty of attention.<sup>1–4</sup> Naturally, the first priority issue in the field of MGs is to clarify the formation mechanism, from which one could design appropriate alloy composition(s) to obtain desired MG(s).<sup>5–8</sup> Previously, several empirical/semiempirical criteria have been proposed and served as guidelines for composition design,<sup>9–12</sup> yet they do not work well for the Al–TM–RE systems, which provide significant exception from many criteria, such as the deep eutectic rule and size difference rule.<sup>2,13,14</sup> As the former criterion is based on the equilibrium phase diagram of a system and the latter is based on the atomic sizes of constituent elements, from the authors' point of view, both starting bases have restrictions in well reflecting the internal characteristics of a system concerned.<sup>15</sup> It is known that the atomic interactions that intrinsically govern the various physical and chemical properties could be reasonably described by the interatomic potential and if a realistic interatomic potential is constructed, most of the properties, including the glass formation compositions, could be determined through relevant computations or simulations.<sup>16–19</sup> It is therefore of relevance to take the interatomic potential as the starting base to develop a model/theory capable of clarifying the metallic glass formation and predicting the favored and even optimized

compositions for obtaining the desired glassy alloys in Al–TM–RE systems.

Meanwhile, glass formation, as well as many other physical and mechanical properties of MGs, is believed to depend on the internal atomic structure, or specifically, the characteristic short- and medium-range order of the alloying elements in the MGs.<sup>20–23</sup> For Al–TM–RE systems, it is revealed that the formation and properties of Al–TM binary systems could be tailored by a minor addition of RE,<sup>1,2</sup> yet the associated microscopic origin remains elusive. This sensitive alloying effect is not a result of bond shortening and covalent-like interactions as that for Al–TM pairs,<sup>24</sup> as the Al–RE bonds are revealed to be typically metallic ones,<sup>25</sup> and it is thereby suggested that this alloying effect is topological in nature. Resolving the atomic structure, particularly detecting the delicate modulation in the topological short- and medium-range order with the addition of RE, would provide a detailed microscopic picture and help elucidate the underlying structural origin. Detailed knowledge about the structure of bulk MGs is not only of pure scientific interest, but if achieved, it would open opportunities to better control the properties of these materials.<sup>26–28</sup>

In this work, the Al–Cu–Y system, which is a significant member of the Al–TM–RE family,<sup>1</sup> is selected as a representative system for investigation. To access atomic details, atomistic simulations, including molecular dynamics (MD) and Monte Carlo (MC), are applied in the present

Received: March 3, 2014

Revised: March 24, 2014

Table 1. Fitted Parameters of the Interatomic Potential for the Al–Cu–Y System<sup>a</sup>

	Al	Cu	Y	Al–Cu	Al–Y	Cu–Y
$p_1$	8.776460	9.625372	7.293850	4.575749	11.36598	13.88520
$A_1$	0.402184	0.315491	0.527193	0.977351	0.320283	0.167359
$r_{m1}$	2.764394	2.124148	3.118844	2.162239	3.895313	3.241637
$n_1$	4	4	4	4	4	4
$p_{1m}$	2.558558	2.860823	2.254337	1.107382	1.415430	1.321704
$A_{1m}$	2.917212	8.049825	2.761409	1.112537	1.741822	9.219811
$r_{c1}$	4.607023	3.634148	6.014946	5.286440	5.204398	4.228998
$p_2$	5.249466	4.903930	3.855623	4.620459	3.536090	4.126924
$A_2$	4.738155	3.854734	8.470387	9.720919	6.520435	5.672301
$r_{m2}$	3.786874	3.611361	2.847003	3.618114	2.906232	2.053752
$n_2$	5	5	5	5	5	5
$p_{2m}$	0.000477	0.000602	0.000578	0.000619	0.000481	0.000845
$A_{2m}$	1.114067	0.458708	5.383636	1.388810	1.687934	8.746285
$r_{c2}$	6.515324	6.215324	7.579420	6.550000	7.511561	5.811771
$r_0$	2.864321	2.553618	3.648736	2.708969	3.256528	3.101177

<sup>a</sup> $A_1$  and  $A_{1m}$  are expressed in eV,  $A_2$  and  $A_{2m}$  are expressed in eV<sup>2</sup>, and  $r_{m1}$ ,  $r_{c1}$ ,  $r_{m2}$ ,  $r_{c2}$ , and  $r_0$  are expressed in Å.

study. The paper proceeds as follows. In section II, a smoothed and long-range second-moment approximation of tight binding (TB-SMA) potential is constructed for the Al–Cu–Y system. In section III, based on the constructed Al–Cu–Y potential, a series of MD simulations are then conducted to identify the composition region that energetically favors the metallic glass formation. In section IV, within the located favored composition region, MC simulations are further carried out to pinpoint the optimized stoichiometries by evaluating a newly formulated parameter that correlates the practical glass forming ability. In section V, atomic structures of the alloys around the optimized stoichiometry, particularly the delicate modulation with addition of Y, are resolved by multiple analytical approaches. Finally, concluding remarks are given in section VI.

## II. CONSTRUCTION OF THE AL–CU–Y INTERATOMIC POTENTIAL

To perform relevant simulations, realistic interatomic potentials are indispensable. To the authors' knowledge, no integrated potential has been published for the Al–Cu–Y system so far. In this study, a set of Al–Cu–Y  $n$ -body potentials are newly constructed under the smoothed and long-range second-moment-approximation of tight-binding (TB-SMA) formalism proposed by the present authors' group.<sup>19</sup>

The smoothed and long-range TB-SMA potential solves the energy “jump” problem when the atom pairs “cross” the cutoff radius<sup>29</sup> by incorporating a binomial truncation function in the original TB-SMA potential,<sup>30,31</sup> and can be written as follows:

$$E_i = \sum_{j \neq i} \phi(r_{ij}) + \sqrt{\sum_{j \neq i} \psi(r_{ij})} \quad (1)$$

$$\phi(r_{ij}) = \begin{cases} A_1 \exp \left[ -p_1 \left( \frac{r_{ij}}{r_0} - 1 \right) \right], & r_{ij} \leq r_{m1} \\ A_{1m} \exp \left[ -p_{1m} \left( \frac{r_{ij}}{r_0} - 1 \right) \right] \left( \frac{r_{c1}}{r_0} - \frac{r_{ij}}{r_0} \right)^{n_1}, & r_{m1} < r_{ij} \leq r_{c1} \end{cases} \quad (2)$$

$$\psi(r_{ij}) =$$

$$\begin{cases} A_2 \exp \left[ -p_2 \left( \frac{r_{ij}}{r_0} - 1 \right) \right], & r_{ij} \leq r_{m2} \\ A_{2m} \exp \left[ -p_{2m} \left( \frac{r_{ij}}{r_0} - 1 \right) \right] \left( \frac{r_{c2}}{r_0} - \frac{r_{ij}}{r_0} \right)^{n_2}, & r_{m2} < r_{ij} \leq r_{c2} \end{cases} \quad (3)$$

where  $E_i$  is the total potential energy of an atom  $i$  and  $\phi$  and  $\psi$  are called here the pair term and density term.  $r_{m1}$  and  $r_{m2}$  are the knots, and  $r_{c1}$  and  $r_{c2}$  are the cutoff radii of the pair term and density term, respectively.  $n_1$  and  $n_2$  are indices which should not be less than 3 and 5, respectively, to avoid discontinuity of the high derivatives.  $A_1$ ,  $p_1$ ,  $A_{1m}$ , and  $p_{1m}$  and  $A_2$ ,  $p_2$ ,  $A_{2m}$ , and  $p_{2m}$  are another eight potential parameters. From eqs 2 and 3, one can see that the pair and density terms as well as their high derivatives could continuously and smoothly go to zero at the cutoff radii  $r_{c1}$  and  $r_{c2}$ , thus removing the “jumps” of total energy and force and avoiding nonphysical behaviors in simulations.<sup>19</sup> In order to totally avoid the discontinuity of the energy, pressure, and force in the whole calculated range, the pair and density terms as well as their first derivatives should also be continuous at the transition knots  $r_{m1}$  and  $r_{m2}$  when fitting the potential parameters.

For the Al–Cu–Y system, there should be six sets of potential parameters, i.e., three sets for Al–Al, Cu–Cu, and Y–Y and three sets for Al–Cu, Al–Y, and Cu–Y. The latter three sets are commonly referred to as cross potentials, which describe the interactions of dissimilar atoms. The potential parameters of Al–Al, Cu–Cu, and Y–Y are determined by fitting them to the cohesive energy, lattice constants, and elastic constants of Al, Cu, and Y metals at 0 K.<sup>32–34</sup> For the cross potentials, the potential of the Al–Cu binary system is extracted from our previous work,<sup>35</sup> and in the present work, the Al–Y and Cu–Y potentials are constructed by fitting to the physical properties of the stable or virtual intermetallic compounds of the binary systems, such as *cF24*-Al<sub>2</sub>Y, *tP20*-Al<sub>2</sub>Y<sub>3</sub>, and *oP12*-AlY<sub>2</sub>. As there are few available data for the related compounds, *ab initio* calculations using the Cambridge serial total energy package (CASTEP)<sup>36,37</sup> based on density functional theory (DFT) are conducted by the authors to derive the necessary physical properties of the compounds.

During the *ab initio* calculations, the exchange-correlation energy functional is described by the well-established Perdew–Wang (PW91) version of the generalized gradient approximation (GGA),<sup>38,39</sup> and the ion–electron interactions are treated by the projector augmented wave (PAW) method.<sup>40</sup> The cutoff energy is chosen to be 500.0 eV, and the Brillouin zone is sampled using the Monkhorst–Pack method<sup>41</sup> with nearly constant *k*-point densities for each calculation, roughly equivalent to a  $12 \times 12 \times 12$  mesh for a conventional fcc unit cell. These parameters are testified to be sufficient for convergence of the calculations for the structures in this work.

We now summarize the fitting results of the proposed Al–Cu–Y potential. Table 1 displays the six sets of the fitted potential parameters. To evaluate the relevance of the potential, Table 2 gives the fitted and experimental<sup>32–34</sup> lattice constants,

**Table 2. Lattice Constants, Cohesion Energies, Elastic Constants, and Bulk Moduli of Al, Cu, and Y That Are Fitted by the Potential (First Line) and Obtained from the Experiments<sup>32–34</sup> or *Ab Initio* Calculations (Second Line)<sup>a</sup>**

	fcc-Al		fcc-Cu		hcp-Y	
	fitted	exp.	fitted	exp.	fitted	exp.
<i>a</i>	4.051	4.050	3.611	3.615	3.650	3.648
<i>c</i>					5.958	5.732
<i>E<sub>c</sub></i>	3.387	3.390	3.502	3.490	4.361	4.370
<i>C<sub>11</sub></i>	0.821	1.067	1.688	1.683	0.639	0.779
<i>C<sub>12</sub></i>	0.705	0.604	1.225	1.221	0.348	0.285
<i>C<sub>13</sub></i>					0.294	0.210
<i>C<sub>33</sub></i>					0.703	0.769
<i>C<sub>44</sub></i>	0.289	0.283	0.745	0.757	0.108	0.243
<i>B<sub>0</sub></i>	0.743	0.722	1.361	1.370	0.428	0.415

<sup>a</sup>Lattice constants *a* and *c* are expressed in Å, cohesive energies *E<sub>c</sub>* in eV/atom, and elastic constants *C<sub>ij</sub>* and bulk moduli *B<sub>0</sub>* in Mbar.

cohesion energies, and elastic constants of Al, Cu, and Y, and Table 3 lists the lattice constants, formation energies, and bulk moduli of the related compounds reproduced by the potential in comparison with the corresponding *ab initio* calculation derived results. It is seen from Tables 2 and 3 that the physical properties obtained by the potential match quite well with the experimental results or the *ab initio* calculations. In the fitting process, the first derivative of energy and the remnant stress of the fitted structures are very small, i.e., less than  $10^{-10}$  Mbar, indicating that the fitted structures are very close to the equilibrium states.

To further evaluate the relevance of the constructed potential in describing atomic interactions under nonequilibrium conditions, the equation of state (EOS) is derived from the

potential and then compared with the frequently used EOS in this field, i.e., the Rose equation, which has been considered to be universal for all categories of solids.<sup>42</sup> Note that the EOSs have not been used in the fitting process. The EOSs of the fcc-Al, fcc-Cu, hcp-Y, cP4-Al<sub>3</sub>Cu, cF24-Al<sub>2</sub>Y, and cP2-CuY are then derived from the potential and exhibited in Figure 1a–f, respectively, together with the corresponding Rose equations. From Figure 1, one can see that the total energies of these structures are smooth and continuous in the entire range without any “jumps” or discontinuities, and the EOSs derived from the proposed potential agree well with the corresponding Rose equations, indicating that the constructed Al–Cu–Y potential could be applied to describe the atomic interactions of the system even far from the equilibrium state.

### III. PREDICTION OF FAVORED GLASS FORMATION REGION

The process of producing the metallic glasses is always a nonequilibrium or even far-from-equilibrium process, and the extremely restricted kinetic condition retards the intermetallic phases, which often have very complicated structures, to nucleate or grow. It follows that the phase competing against the amorphous phase is the solid solution with one of the three simple structures, i.e., fcc, hcp, or bcc. This viewpoint has been supported by a large number of research results from both experimental and theoretical aspects.<sup>15,43–45</sup> Consequently, the issue related to predicting the glass formation region of the Al–Cu–Y system in our study could be converted into a scientific issue of comparing the relative stability of the solid solution versus its amorphous counterpart as a function of alloy composition, by applying the solid solution model.<sup>15</sup>

The constructed and proven realistic Al–Cu–Y potential is then applied in a series of MD simulations over the entire composition triangle employing the solid solution models. As the stable crystalline structures of Al, Cu, and Y at the simulated temperature (300 K) are fcc, fcc, and hcp, respectively, therefore two types of solid solution models, i.e., fcc and hcp, are established. Each solid solution model consists of 6912 atoms, with periodic boundary conditions adopted in three Cartesian directions. In setting up the solid solution models, solute atoms are added by random substitution of a certain number of solvent atoms to obtain a desired concentration. The constructed solid solution models are then annealed with the Parrinello–Rahman constant pressure scheme<sup>46</sup> at zero pressure and 300 K for about 10 ns, which is sufficient for the models to be fully relaxed. Structural changes in these models are monitored by the atomic configuration that visually reflects the state of the system and the structure factor, *S*(*q*),

**Table 3. Potential Reproduced (First Line) and *Ab Initio* Derived Properties (Second Line) of Al–Cu,<sup>35</sup> Al–Y, and Cu–Y Compounds<sup>a</sup>**

compounds	Al <sub>3</sub> Cu	Al <sub>2</sub> Cu	AlCu <sub>3</sub>	Al <sub>2</sub> Y	Al <sub>2</sub> Y <sub>3</sub>	AlY <sub>2</sub>	Cu <sub>3</sub> Y	Cu <sub>2</sub> Y	CuY	CuY <sub>3</sub>
space group	<i>Pm</i> $\bar{3}$ <i>m</i>	<i>I4/mcm</i>	<i>Pm</i> $\bar{3}$ <i>m</i>	<i>Fd</i> $\bar{3}$ <i>m</i>	<i>P4</i> $\bar{2}$ / <i>mmn</i>	<i>Pnma</i>	<i>F4</i> $\bar{3}$ <i>m</i>	<i>Imma</i>	<i>Pm</i> $\bar{3}$ <i>m</i>	<i>Pm</i> $\bar{3}$ <i>m</i>
<i>a</i> or <i>a</i> , <i>c</i> or <i>a</i> , <i>b</i> , <i>c</i>	4.009	5.997, 5.083	3.700	8.080	8.451, 7.778	6.879, 5.2354, 9.663	6.483	4.311, 6.975, 7.396	3.456	3.547
	3.939	6.067, 4.877	3.696	7.910	8.280, 7.678	6.652, 5.130, 9.543	6.497	4.305, 6.956, 7.481	3.517	3.607
<i>E<sub>f</sub></i>	3.494	3.623	3.660	4.227	4.334	4.353	3.720	3.949	4.137	3.974
	3.493	3.623	3.658	4.242	4.331	4.349	3.720	4.018	4.138	3.974
<i>B<sub>0</sub></i>	0.590	0.681	0.862	0.933	0.787	0.702	1.322	1.180	1.057	0.520
	0.611	0.792	1.253	0.856	0.717	0.614	1.048	0.976	0.868	0.488

<sup>a</sup>Lattice constants *a*, *b*, and *c* are expressed in Å, cohesive energies *E<sub>c</sub>* in eV/atom, and bulk moduli *B<sub>0</sub>* in Mbar.



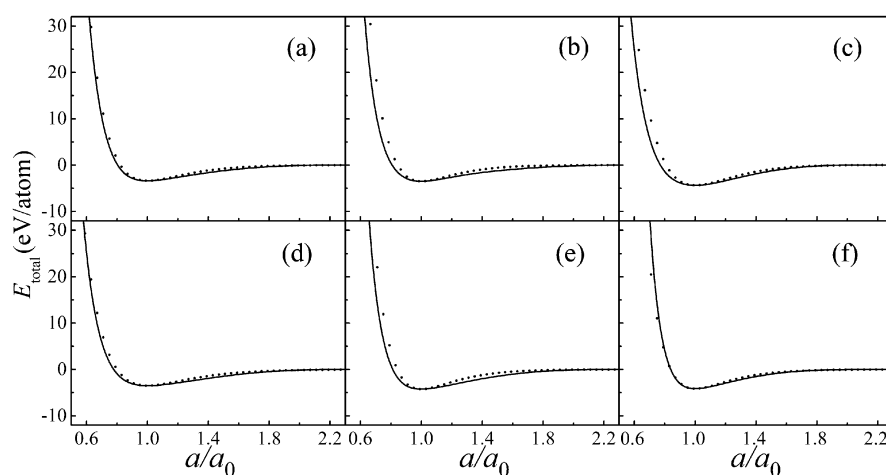


**Figure 1.** Equations of state (EOSs) calculated from the constructed potential (solid lines) and Rose equation (dotted lines) for (a) *fcc*-Al, (b) *fcc*-Cu, (c) *hcp*-Y, (d) *cP4*-Al<sub>3</sub>Cu, (e) *cF24*-Al<sub>2</sub>Y, and (f) *cP2*-CuY.

which is recognized as firm evidence to identify the amorphous phase. The  $S(q)$  can be calculated by

$$S(q) = \frac{1}{N} \left\langle \left| \sum_{k=1}^N b_k \exp(i\vec{q} \cdot \vec{r}_k) \right|^2 \right\rangle \quad (4)$$

where  $i = (-1)^{1/2}$ ,  $N$  is the number of atoms,  $\vec{q}$  is the scattering vector, and  $b_k$  and  $\vec{r}_k$  are the scattering length and position vector of atom  $k$ , respectively. One notes that the  $S(q)$  calculated by eq 4 is not normalized.

We now present the simulation results of the Al–Cu–Y system. After adequate MD simulation time, the initially constructed solid solution models reach a relatively stable state; i.e., the drifts for all the related dynamic variables are negligible. Inspecting the simulation results, these models exhibit two different states with varying compositions, i.e., either preserving the initial crystalline state or collapsing into an amorphous state. We take two alloys, i.e., Al<sub>80</sub>Cu<sub>20</sub> and Al<sub>80</sub>Cu<sub>10</sub>Y<sub>10</sub>, in the Al-rich corner as examples. Figure 2 shows the  $S(q)$ s and atomic position projections for these two alloys, respectively. From Figure 2a, one can see that the  $S(q)$  curve of Al<sub>80</sub>Cu<sub>20</sub> features apparent crystalline peaks, suggesting a long-range ordered feature, which is evidenced by the atomic position projection in Figure 2b. For Al<sub>80</sub>Cu<sub>10</sub>Y<sub>10</sub> with 10% Y addition, as is seen in Figure 2c, all the peaks beyond the second have smeared out, exhibiting a typical short-range ordered and long-range disordered feature. This is also evidenced by Figure 2d, indicating that the original crystalline lattice has spontaneously collapsed and turned into a completely amorphous state. It can be assumed that, when solute atoms dissolve into the ideal solid solution lattice, an atomic-level stress would be introduced by the distinct atomic sizes and chemical interactions among constituent atoms. The relaxation of this atomic-level stress would result in a certain degree of lattice distortion, and once the solute concentration exceeds a critical value, the severe distortion would trigger a collective collapse of the crystalline lattice, turning into a more topologically stabilized amorphous state, to relax the stress and reduce the energy of the system. In other words, the physical origin of the solid-state crystal-to-amorphous transition is the spontaneous collapsing of the crystalline lattice while the solute atoms exceed a critical value, i.e., the critical solid solubility.

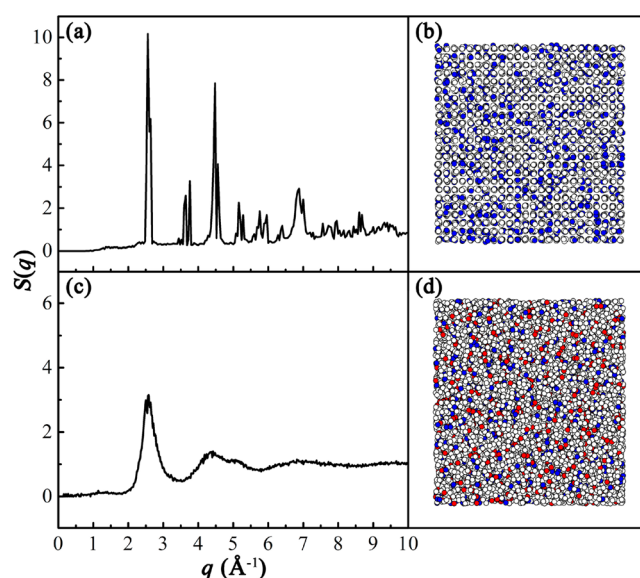


**Figure 2.** Structural factors and atomic position projections for (a, b) the crystalline state (Al<sub>80</sub>Cu<sub>20</sub>) and (c, d) the amorphous state (Al<sub>80</sub>Cu<sub>10</sub>Y<sub>10</sub>). Open circles are for Al, blue solid circles for Cu, and red solid circles for Y.

Simulations over the entire Al–Cu–Y composition triangle allow us to construct the glass formation stoichiometry diagram in Figure 3a. According to the structural factors  $S(q)$ s and atomic position projections of each specific alloy, we split the composition triangle into four regions by three critical solubility lines AB, CD, and EF. When an alloy composition locates beyond the lines and moves toward one of the three corners, the crystalline structure could remain stable. These regions are consequently classified as the crystalline regions. When the composition falls into the central hexagonal region, enclosed by ABCDEF, the crystalline structure would become unstable and spontaneously collapses into an amorphous state. This hexagonal region is therefore defined as the amorphous region or glass formation region (GFR) of the Al–Cu–Y system, and within this region, metallic glass formation is energetically favored. The present authors also propose to name this predicted region as the *quantitative* glass formation ability of the Al–Cu–Y system. To validate the predicted GFR, experimental

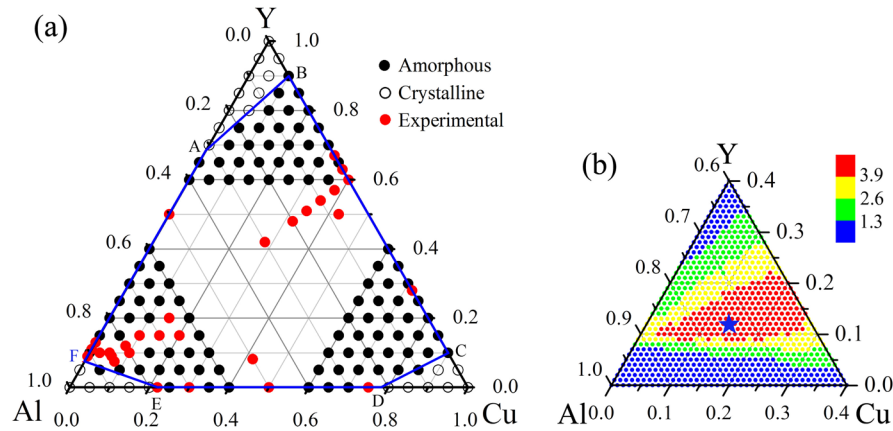


**Figure 3.** (a) Glass formation stoichiometry diagram derived from MD simulations at 300 K for the ternary Al–Cu–Y system. (b) Contour map of the newly formulated parameter  $\bar{\gamma}$  derived from MD and MC simulations at 300 K for the  $\text{Al}_x\text{Cu}_y\text{Y}_{100-x-y}$  ( $x = 60\text{--}100$ ,  $y = 0\text{--}40$ ) MGs. The blue asterisk pinpoints the optimized stoichiometry of  $\text{Al}_{74}\text{Cu}_{14}\text{Y}_{12}$ , at which  $\bar{\gamma}$  reaches its local maximum.

observations reported so far in the literature are extensively collected<sup>1,2,47–49</sup> and marked by the red dots in Figure 3a. It is seen that these experimentally measured glass formation compositions mostly fall within the predicted hexagonal region, suggesting that the results predicted by MD simulations for the Al–Cu–Y system are quite reasonable.

#### IV. OPTIMIZATION OF GLASS FORMING STOICHIOMETRIES

The glass formation stoichiometry diagram in Figure 3a enables one to conveniently predict the possibility of glass formation at a given composition, but it is not sufficient to guide the composition design, as it does not depict the ease or difficulty in obtaining MGs at a certain composition. Thus, we proceed to pinpoint the optimized stoichiometries inside the determined glass formation region.

Considering that Al-rich MGs are of primary technical interest to achieve a good combination of the formability and ductility,<sup>2</sup> we focus on the Al-rich corner, i.e.,  $\text{Al}_x\text{Cu}_y\text{Y}_{100-x-y}$  ( $x = 60\text{--}100$ ,  $y = 0\text{--}40$ ) alloys to search for the locally optimized stoichiometries. From the perspective of thermodynamics, the formation enthalpy difference between the amorphous and solid solution phases serves as the driving force for amorphization, while the formation enthalpy of the competing solid solution phase acts as the resistance for amorphization, we therefore formulate a parameter,  $\bar{\gamma}$ , from the atomistic simulations to correlate the driving force with the ease of glass formation, and it can be expressed by

$$\bar{\gamma} = \frac{\Delta H^{\text{amorph}}}{\Delta H^{\text{ss}}} = \frac{\Delta H^{\text{am}} - \Delta H^{\text{ss}}}{\Delta H^{\text{ss}}} \quad (5)$$

where  $\Delta H^{\text{am}}$  and  $\Delta H^{\text{ss}}$  are formation enthalpies of the amorphous and solid solution phases, respectively. Note this parameter could be considered as a comparative measure of the technically used glass forming ability<sup>50</sup> of a specific glassy alloy. For example, assuming the cooling speed is fixed, the larger the parameter, the larger the size of the obtainable MG. It follows that, in a metal system, the largest  $\bar{\gamma}$  could be correlated to the optimized stoichiometries, of which the metallic glass could be the most stable or easiest attainable in practice.

In determining  $\bar{\gamma}$ , the formation enthalpy  $\Delta H^{\text{am}}$  of the  $\text{Al}_x\text{Cu}_y\text{Y}_{1-x-y}$  amorphous phase could be calculated from MD simulations in the previous section. Assume that  $E_{\text{am}}$  is the

energy per atom of the amorphous phase and  $E_{\text{Al}}$ ,  $E_{\text{Cu}}$ , and  $E_{\text{Y}}$  are the lattice energies of Al, Cu, and Y, respectively.<sup>51</sup> Then  $\Delta H^{\text{am}}$  could be calculated by

$$\Delta H^{\text{am}} = E_{\text{am}} - [xE_{\text{Al}} + yE_{\text{Cu}} + (1 - x - y)E_{\text{Y}}] \quad (6)$$

However, for the solid solutions, there may be difficulties in calculating the formation enthalpy  $\Delta H^{\text{ss}}$  through MD simulations, because when the composition falls in the amorphous region of the stoichiometry diagram (Figure 3a), the solid solution models would become unstable and spontaneously collapse into the amorphous state. To solve this problem, an efficient and relevant Monte Carlo (MC) scheme<sup>52</sup> is then applied to optimize the solid solutions and derive the formation enthalpy. Differently from the MD simulation process, the “moves” in MC simulations are divided into two types, i.e., atom displacement and box deformation. To optimize the supersaturated solid solutions, the MC box is set to be fixed, i.e., retaining the initial crystalline structures, and only atom displacement could take place in the process. During MC simulations, the solid solution models are set up in the same way as in MD simulations, and the models are then relaxed within the isothermal–isobaric ensemble at 300 K and zero pressure for adequate times to optimize the solid solutions so as to find the minimum energies at different compositions. Assume that  $E_{\text{min}}$  is the minimum energy per atom of the  $\text{Al}_x\text{Cu}_y\text{Y}_{1-x-y}$  solid solutions, the formation enthalpy  $\Delta H^{\text{ss}}$  of the  $\text{Al}_x\text{Cu}_y\text{Y}_{1-x-y}$  solid solutions could then be expressed by

$$\Delta H^{\text{ss}} = E_{\text{min}} - [xE_{\text{Al}} + yE_{\text{Cu}} + (1 - x - y)E_{\text{Y}}] \quad (7)$$

On the basis of the calculated results from MD and MC simulations, the contour map of  $\bar{\gamma}$  for the  $\text{Al}_x\text{Cu}_y\text{Y}_{100-x-y}$  ( $x = 60\text{--}100$ ,  $y = 0\text{--}40$ ) MGs is plotted in Figure 3b. Upon inspection of Figure 3b, the compositions marked by red dots have a much larger  $\bar{\gamma}$  than other regions, and within this region, the stoichiometry of  $\text{Al}_{74}\text{Cu}_{14}\text{Y}_{12}$  marked by a blue asterisk is characterized with maximum  $\bar{\gamma}$ , suggesting that glassy alloys around  $\text{Al}_{74}\text{Cu}_{14}\text{Y}_{12}$  could be most thermally stable or easily attainable. Thus, the locally optimized stoichiometries for metallic glass formation in the Al-rich corner can be pinpointed around  $\text{Al}_{74}\text{Cu}_{14}\text{Y}_{12}$ .

It is interesting and important to compare the present results with the experimental observations reported in the literature. Referring back to Figure 3a, one can see that the experimentally identified glass formation compositions in the Al-rich corner are

densely clustered around  $\text{Al}_{74}\text{Cu}_{14}\text{Y}_{12}$ , suggesting that the predictions derived directly from the constructed interatomic potential through atomistic simulations are well supported by the experimental observations and prediction of favored and optimized compositions starting from a realistic interatomic potential for a ternary metal system is an appropriate scheme. Moreover, from a physical viewpoint, the predicted favored and optimized compositions are calculated from the realistic interatomic potential, which governs the atomic configurations and, thus, in turn, governs the energetic states of both the solid solution and the amorphous phase of the system. Therefore, it also lends additional support to the relevance of our constructed Al–Cu–Y potential.

## V. ATOMIC STRUCTURE CHARACTERIZATION OF OPTIMIZED STOICHIOMETRY

For the pinpointed optimized glass former  $\text{Al}_{74}\text{Cu}_{14}\text{Y}_{12}$ , we then elucidate its internal structural characteristics, particularly the modulation in the short- to medium-range order with addition of Y, to clarify the structural origin underlying its optimum glass forming ability.

The short-range order (SRO) is analyzed as a preliminary step. The Voronoi tessellation method,<sup>53</sup> which is widely used to characterize the local environments in the amorphous phase, is employed. In the present Voronoi analyses, cell faces with smaller than 5% of the average face area are neglected to minimize the degeneracy problem and thermal vibration effects.<sup>54</sup> Figure 4 displays the spectrum of coordination

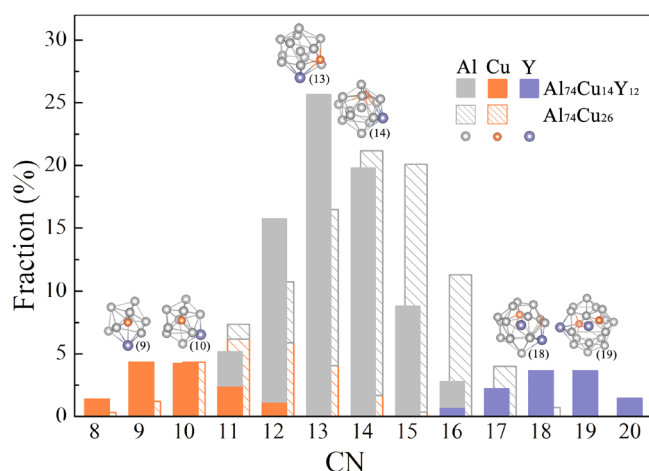


**Figure 4.** Spectrum of coordination numbers (CNs) in the optimized  $\text{Al}_{74}\text{Cu}_{14}\text{Y}_{12}$  MG (solid bars) and in the referenced  $\text{Al}_{74}\text{Cu}_{26}$  MG (crossed bars), respectively. It is seen that the CNs in  $\text{Al}_{74}\text{Cu}_{14}\text{Y}_{12}$  are well-distributed over a wide range, with three types of atoms covering different scopes of the whole landscape, while the CNs in  $\text{Al}_{74}\text{Cu}_{26}$  are more centralized. The topologies of the dominant clusters centered with Cu, Al, and Y, respectively, with different sizes and CNs (listed in parentheses) as frequently found in  $\text{Al}_{74}\text{Cu}_{14}\text{Y}_{12}$  are also exhibited.

numbers (CNs) in the optimized MG, i.e.,  $\text{Al}_{74}\text{Cu}_{14}\text{Y}_{12}$ , and in a referenced MG, i.e.,  $\text{Al}_{74}\text{Cu}_{26}$ . It is seen that the CNs in  $\text{Al}_{74}\text{Cu}_{14}\text{Y}_{12}$  are well-distributed over a quite wide range, with the three types of atoms covering different scopes of the whole landscape, i.e., Cu dominates in CNs of 8–10 with an average of 9.5, Al dominates in 12–15 with an average of 13.2, while Y dominates in 17–20 with an average of 18.3. This can be understood in terms of the atomic size difference; i.e., the relatively larger atomic size of Y permits accommodating more

atoms in the nearest-neighboring shells and leads to larger CNs, followed by Al, and then Cu. The dense clustering of small-sized and large-sized clusters would lead to the efficient filling of space and the enhancement of stability. Comparatively, the CN spectrum of  $\text{Al}_{74}\text{Cu}_{26}$  is more centralized, mainly in the range 11–16. This evidences that adding Y in Al–Cu binary broadens the short-range landscape and thus creates more opportunities for space tiling. Meanwhile, the mixing enthalpies of Y–Al and Y–Cu are  $-31$  and  $-22$  kJ/mol, much larger than  $-1$  kJ/mol for Al–Cu,<sup>11</sup> and these large negative values would reduce the total energy of system, enhance the interactions of components, and restrain long-range atomic diffusion.<sup>24</sup> In Figure 4, the topologies of dominant clusters centered with Cu, Al, and Y, respectively, with different CNs as frequently found in  $\text{Al}_{74}\text{Cu}_{14}\text{Y}_{12}$  are also displayed. Due to the major content of Al and the negative mixing enthalpies of Cu–Al and Y–Al, the Cu and Y atoms, as solutes, are mainly surrounded by solvent Al as nearest-neighbors, mostly forming Kasper-type<sup>55</sup> clusters. These solute Cu- and Y-centered clusters could be viewed as quasi-equivalent clusters<sup>56</sup> and serve as basic building blocks<sup>57–59</sup> in  $\text{Al}_{74}\text{Cu}_{14}\text{Y}_{12}$ .

As is declared above, the solute Cu- and Y-centered clusters could be considered as building blocks, or structural units, in  $\text{Al}_{74}\text{Cu}_{14}\text{Y}_{12}$ . Thus, a plausible interpretation of medium-range order (MRO) could be resolved by characterizing the “sublattice” formed by these solute-centered clusters. In MRO, the local clusters mainly correlate with their neighboring clusters through four types of linkages, i.e., vertex (VS), edge (ES), face (FS), and tetrahedra sharing (TS). Under analysis, it is revealed that, in  $\text{Al}_{74}\text{Cu}_{14}\text{Y}_{12}$ , Cu-centered clusters typically have 10–13 solute-centered clusters as neighbors, while the Y-centered clusters have 15–18 clusters around. The average populations of VS, ES, FS, and TS links, respectively, around Cu and Y clusters are then analyzed and exhibited in Figure 5a. One can see that the populations of VS and ES links around Cu and Y clusters are alike, while, for Y clusters, the FS and TS links, which are more energetically favored and structurally stabilized,<sup>25</sup> also occupy large fractions, thus suggesting that the packing around Y clusters is more compact. Further characterizing the topological arrangement of the solute-centered clusters, it is found that 5-fold (icosahedral-like) arrangements are abundant around both Cu and Y clusters, while the more compact packing around Y clusters allows the higher-coordinated 6-fold (fcc-like) arrangements to shape, thereby generating a hybridized packing mode in  $\text{Al}_{74}\text{Cu}_{14}\text{Y}_{12}$ . Figure 5b illustrates the typical packing around Cu and Y clusters, respectively, of which the representative 5-fold and 6-fold arrangements are highlighted. It is thus implied that, despite the fact that the previously proposed icosahedral-like or fcc-like packing models<sup>56,60</sup> capture the nature of MRO, i.e., the dense and efficient packing,<sup>27</sup> a single model may still be oversimplified and incapable of reflecting the packing details in MRO, which has its intrinsic fluctuation. As for the Al–Cu–Y system, the distinct atomic sizes and multiple chemical interactions generate a hybridized icosahedral- and fcc-like packing mode in MRO. Such a dense and flexible packing mode would increase the packing efficiency and open more possibilities to attain an optimum state with low energy and enhanced stability. Packing details of the highlighted fcc-like arrangement around the Y cluster in Figure 5b are further exhibited in Figure 5c. It is seen that the intercluster correlation adopts an fcc-like arrangement, via VS, ES, FS, and TS schemes.



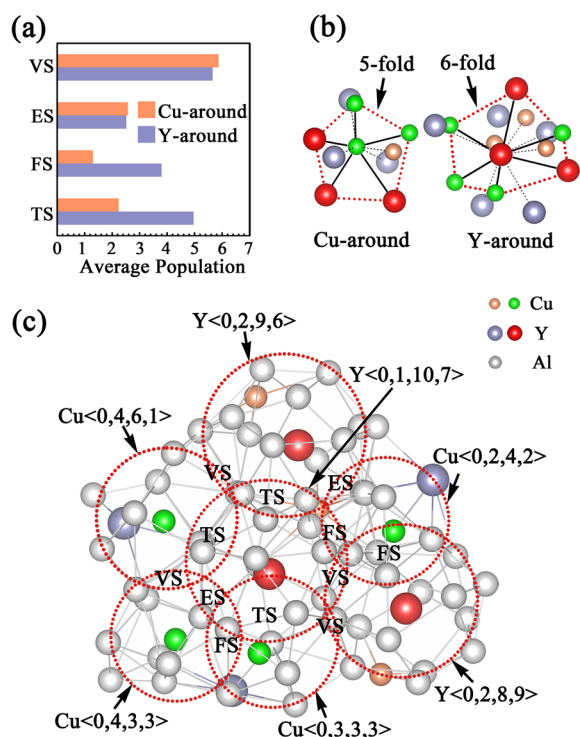


**Figure 5.** (a) Average populations of vertex (VS), edge (ES), face (FS), and tetrahedra sharing (TS) links, respectively, around the Cu and Y clusters with their neighboring solute-centered clusters in  $\text{Al}_{74}\text{Cu}_{14}\text{Y}_{12}$ . (b) Typical packing of solute-centered clusters around the Cu and Y clusters, of which the representative 5-fold (icosahedral-like) and 6-fold (fcc-like) arrangements are highlighted. Only central atoms of the clusters are plotted to obtain a clear presentation. (c) Packing details of the highlighted 6-fold (fcc-like) arrangement of neighboring solute-centered clusters around the Y cluster in part b. It is seen that the intercluster correlation adopts an fcc-like arrangement, via VS, ES, FS, and TS schemes.

The extension of MRO would eventually lead to constitute a percolated network that fulfills the whole space in MGs.

## VI. CONCLUDING REMARKS

In summary, we propose to take the constructed Al–Cu–Y  $n$ -body potential as the starting base and conduct relevant simulations to clarify the formation mechanism and predict the favored and optimized compositions for obtaining desired glassy alloys in the Al–Cu–Y ternary system. Simulations not only predict an energetically favored hexagonal region, which is further defined as the glass formation region, or the quantitative glass formation ability of the system, but also pinpoint the locally optimized stoichiometries as nearby  $\text{Al}_{74}\text{Cu}_{14}\text{Y}_{12}$ , by formulating a parameter for each glassy alloy to correlate the readiness of its forming ability in practice. The predictions are well supported by experimental observations and could be of great help in the systematic composition design of the glassy alloys. Furthermore, structural analysis indicates that addition of Y extends the short-range landscape and facilitates the development of a hybridized icosahedral- and fcc-like packing in medium range, thus interpreting the structural origin underlying the glass formation ability of the system.

## AUTHOR INFORMATION

### Corresponding Author

\*Phone: +86 10 6277 2557. Fax: +86 10 6277 1160. E-mail: dmslbx@tsinghua.edu.cn.

### Notes

The authors declare no competing financial interest.

## ACKNOWLEDGMENTS

The authors are grateful for the financial support from the National Natural Science Foundation of China (51131003), the Ministry of Science and Technology of China (973 Program 2011CB606301, 2012CB825700), and the Administration of Tsinghua University.

## REFERENCES

- (1) Inoue, A.; Ohtera, K.; Tsai, A.-P.; Masumoto, T. New Amorphous Alloys with Good Ductility in Al–Y–M and Al–La–M (M = Fe, Co, Ni or Cu) Systems. *Jpn. J. Appl. Phys.* **1988**, *27*, 280–282.
- (2) Inoue, A. Amorphous, nanoquasicrystalline and nanocrystalline alloys in Al-based systems. *Prog. Mater. Sci.* **1998**, *43*, 365–520.
- (3) Mansour, A. N.; Marcelli, A.; Cibin, G.; Yalovega, G.; Sevastyanova, T.; Soldatov, A. V. Amorphous  $\text{Al}_{90}\text{Fe}_x\text{Ce}_{10-x}$  alloys: X-ray absorption analysis of the Al, Fe and Ce local atomic and electronic structures. *Phys. Rev. B* **2002**, *65*, 134207-1–134207-8.
- (4) Ahn, K.; Louca, D.; Poon, S. J.; Shiflet, G. J. Topological and chemical ordering induced by Ni and Nd in  $\text{Al}_{87}\text{Ni}_7\text{Nd}_6$  metallic glass. *Phys. Rev. B* **2004**, *70*, 224103-1–224103-7.
- (5) Li, Y.; Guo, Q.; Kalb, J. A.; Thompson, C. V. Matching Glass-Forming Ability with the Density of the Amorphous Phase. *Science* **2008**, *322*, 1816–1819.
- (6) Li, J. H.; Dai, X. D.; Liang, S. H.; Tai, K. P.; Kong, Y.; Liu, B. X. Interatomic potentials of the binary transition metal systems and some applications in materials physics. *Phys. Rep.* **2008**, *455*, 1–134.
- (7) Wang, T. L.; Li, J. H.; Liu, B. X. Proposed thermodynamic method to predict the glass formation of the ternary transition metal systems. *Phys. Chem. Chem. Phys.* **2009**, *11*, 2371–2373.
- (8) Cui, Y. Y.; Wang, T. L.; Li, J. H.; Dai, Y.; Liu, B. X. Thermodynamic calculation and interatomic potential to predict the favored composition region for the Cu–Zr–Al metallic glass formation. *Phys. Chem. Chem. Phys.* **2011**, *13*, 4103–4108.
- (9) Turnbull, D. Under what conditions can a glass be formed? *Contemp. Phys.* **1969**, *10*, 473–488.
- (10) Egami, T.; Waseda, Y. Atomic size effect on the formability of metallic glasses. *J. Non-Cryst. Solids* **1984**, *64*, 113–134.
- (11) De Boer, F. R.; Boom, R.; Mattens, W.; Miedema, A.; Niessen, A. *Cohesion in Metals: Transition Metal Alloys*; Elsevier Science Publishers B.V.: Amsterdam, The Netherlands, 1988.
- (12) Inoue, A.; Takeuchi, A. High strength bulk amorphous alloys. *Mater. Trans., JIM* **2002**, *43*, 1892–1906.
- (13) Sun, S. P.; Yi, D. Q.; Liu, H. Q.; Zang, B.; Jiang, Y. Calculation of glass forming ranges in Al–Ni–RE (Ce, La, Y) ternary alloys and their sub-binaries based on Miedema's model. *J. Alloys Compd.* **2010**, *506*, 377–387.
- (14) Egami, T.; Ojha, M.; Nicholson, D. M.; Louzguine-Luzgin, D. V.; Chen, N.; Inoue, A. Glass formability and the Al–Au system. *Philos. Mag.* **2011**, *92*, 655–665.
- (15) Li, J. H.; Dai, Y.; Cui, Y. Y.; Liu, B. X. Atomistic theory for predicting the binary metallic glass formation. *Mater. Sci. Eng., R* **2011**, *72*, 1–28.
- (16) Cui, Y. Y.; Li, J. H.; Dai, Y.; Liu, B. X. Prediction of Favored and Optimized Compositions for Cu–Zr–Ni Metallic Glasses by Interatomic Potential. *J. Phys. Chem. B* **2011**, *115*, 4703–4708.
- (17) Dai, Y.; Li, J. H.; Che, X. L.; Liu, B. X. Proposed Long-Range Empirical Potential To Study the Metallic Glasses in the Ni–Nb–Ta System. *J. Phys. Chem. B* **2009**, *113*, 7282–7290.
- (18) Liang, S. H.; Dai, Y.; Li, J. H.; Liu, B. X. Glass Forming Region of Cu–Ti–Hf Ternary Metal System Derived from the  $n$ -Body



Potential through Molecular Dynamics Simulation. *J. Phys. Chem. B* **2010**, *114*, 9540–9545.

(19) Li, J. H.; Dai, Y.; Dai, X. D. Long-range n-body potential and applied to atomistic modeling the formation of ternary metallic glasses. *Intermetallics*. **2012**, *31*, 292–320.

(20) Yavari, A. R. Materials science: A new order for metallic glasses. *Nature* **2006**, *439*, 405–406.

(21) Schober, H. R. Diffusion in a model metallic glass: Heterogeneity and ageing. *Phys. Chem. Chem. Phys.* **2004**, *6*, 3654–3658.

(22) Seyboldt, R.; Hajnal, D.; Weysser, F.; Fuchs, M. Shear moduli of two dimensional binary glasses. *Soft Matter* **2012**, *8*, 4132–4140.

(23) Bednarcik, J.; Michalik, S.; Kolesar, V.; Rutt, U.; Franz, H. In situ XRD studies of nanocrystallization of Fe-based metallic glass: a comparative study by reciprocal and direct space methods. *Phys. Chem. Chem. Phys.* **2013**, *15*, 8470–8479.

(24) Cheng, Y. Q.; Ma, E.; Sheng, H. W. Atomic Level Structure in Multicomponent Bulk Metallic Glass. *Phys. Rev. Lett.* **2009**, *102*, 245501-1–245501-4.

(25) Lee, M.; Lee, C.-M.; Lee, K.-R.; Ma, E.; Lee, J.-C. Networked interpenetrating connections of icosahedra: Effects on shear transformations in metallic glass. *Acta Mater.* **2011**, *59*, 159–170.

(26) Jóvári, P.; Saksl, K.; Pryds, N.; Lebech, B.; Bailey, N. P.; Møller, G.; Delaplane, R. G.; Franz, H. Atomic structure of glassy Mg<sub>60</sub>Cu<sub>30</sub>Y<sub>10</sub> investigated with EXAFS, x-ray and neutron diffraction, and reverse Monte Carlo simulations. *Phys. Rev. B* **2007**, *76*, 054208-1–054208-8.

(27) Cheng, Y. Q.; Ma, E. Atomic-level structure and structure–property relationship in metallic glasses. *Prog. Mater. Sci.* **2011**, *56*, 379–473.

(28) Hirata, A.; Guan, P.; Fujita, T.; Hirotsu, Y.; Inoue, A.; Yavari, A. R.; Sakurai, T.; Chen, M. Direct observation of local atomic order in a metallic glass. *Nat. Mater.* **2011**, *10*, 28–33.

(29) Frenkel, D.; Smit, B. *Understanding molecular simulation: from algorithms to applications*; Academic Press: New York, 2001.

(30) Li, J. H.; Dai, X. D.; Wang, T. L.; Liu, B. X. A binomial truncation function proposed for the second-moment approximation of tight-binding potential and application in the ternary Ni–Hf–Ti system. *J. Phys.: Condens. Matter* **2007**, *19*, 086228-1–086228-14.

(31) Rosato, V.; Guillope, M.; Legrand, B. Thermodynamical and structural properties of f.c.c. transition metals using a simple tight-binding model. *Philos. Mag. A* **1989**, *59*, 321–336.

(32) Kittel, C.; McEuen, P. *Introduction to solid state physics*; Wiley: New York, 1996.

(33) Lide, D. R.; Bruno, T. J. *CRC Handbook of Chemistry and Physics*; CRC Press: New York, 2012.

(34) Wang, Y.; Curtarolo, S.; Jiang, C.; Arroyave, R.; Wang, T.; Ceder, G.; Chen, L. Q.; Liu, Z. K. Ab initio lattice stability in comparison with CALPHAD lattice stability. *CALPHAD: Comput. Coupling Phase Diagrams Thermochem.* **2004**, *28*, 79–90.

(35) Cui, Y. Y.; Li, J. H.; Dai, Y.; Liu, B. X. Interatomic potential to calculate the driving force, optimized composition, and atomic structure of the Cu–Hf–Al metallic glasses. *Appl. Phys. Lett.* **2011**, *99*, 011911-3.

(36) Segall, M. D.; Philip, J. D. L.; Probert, M. J.; Pickard, C. J.; Hasnip, P. J.; Clark, S. J.; Payne, M. C. First-principles simulation: ideas, illustrations and the CASTEP code. *J. Phys.: Condens. Matter* **2002**, *14*, 2717.

(37) Clark, S. J.; Segall, M. D.; Pickard, C. J.; Hasnip, P. J.; Probert, M. I. J.; Refson, K.; Payne, M. C. First principles methods using CASTEP. *Z. Kristallogr. - Cryst. Mater.* **2005**, *220*, 567–570.

(38) Perdew, J. P.; Chevary, J. A.; Vosko, S. H.; Jackson, K. A.; Pederson, M. R.; Singh, D. J.; Fiolhais, C. Atoms, molecules, solids, and surfaces: Applications of the generalized gradient approximation for exchange and correlation. *Phys. Rev. B* **1992**, *46*, 6671–6687.

(39) Perdew, J. P.; Burke, K.; Ernzerhof, M. Generalized Gradient Approximation Made Simple. *Phys. Rev. Lett.* **1996**, *77*, 3865–3868.

(40) Blöchl, P. E. Projector augmented-wave method. *Phys. Rev. B* **1994**, *50*, 17953–17979.

(41) Monkhorst, H. J.; Pack, J. D. Special points for Brillouin-zone integrations. *Phys. Rev. B* **1976**, *13*, 5188–5192.

(42) Rose, J. H.; Smith, J. R.; Guinea, F.; Ferrante, J. Universal features of the equation of state of metals. *Phys. Rev. B* **1984**, *29*, 2963–2969.

(43) Liu, B. X.; Lai, W. S.; Zhang, Q. Irradiation induced amorphization in metallic multilayers and calculation of glass-forming ability from atomistic potential in the binary metal systems. *Mater. Sci. Eng., R* **2000**, *29*, 1–48.

(44) Sheng, H. W.; Wilde, G.; Ma, E. The competing crystalline and amorphous solid solutions in the Ag–Cu system. *Acta Mater.* **2002**, *50*, 475–488.

(45) López, J. M.; Alonso, J. A.; Gallego, L. J. Determination of the glass-forming concentration range in binary alloys from a semi-empirical theory: Application to Zr-based alloys. *Phys. Rev. B* **1987**, *36*, 3716–3722.

(46) Parrinello, M.; Rahman, A. Polymorphic transitions in single crystals: A new molecular dynamics method. *J. Appl. Phys.* **1981**, *52*, 7182–7190.

(47) Idzikowski, B.; Mielcarek, S.; Misiuna, P.; Śniadecki, Z.; Brańka, A. C. Mechanical properties of amorphous and partially crystallized Y<sub>50</sub>Cu<sub>42</sub>Al<sub>8</sub> alloys. *Intermetallics*. **2012**, *21*, 75–79.

(48) Yan, H.; Gan, F.; Huang, D. Evaporated Cu–Al amorphous alloys and their phase transition. *J. Non-Cryst. Solids*. **1989**, *112*, 221–227.

(49) Satta, M.; Rizzi, P.; Baricco, M. Glass-formation and hardness of Cu–Y alloys. *J. Alloys Compd.* **2009**, *483*, 50–53.

(50) Schroers, J. Bulk Metallic Glasses. *Phys. Today* **2013**, *66*, 32–37.

(51) Xing, L. Q.; Hufnagel, T. C.; Eckert, J.; Löser, W.; Schultz, L. Relation between short-range order and crystallization behavior in Zr-based amorphous alloys. *Appl. Phys. Lett.* **2000**, *77*, 1970–1972.

(52) Dai, X. D.; Li, J. H.; Liu, B. X. Molecular statics calculation of the formation enthalpy for ternary metal systems based on the long-range empirical interatomic potentials. *Appl. Phys. Lett.* **2007**, *90*, 131904-1–131904-3.

(53) Finney, J. L. Random Packings and the Structure of Simple Liquids. I. The Geometry of Random Close Packing. *Proc. R. Soc. London, Ser. A* **1970**, *319*, 479–493.

(54) Li, J.; Zhao, S.; Dai, Y.; Cui, Y.; Liu, B. Formation and structure of Al–Zr metallic glasses studied by Monte Carlo simulations. *J. Appl. Phys.* **2011**, *109*, 113538-1–113538-14.

(55) Frank, F. C.; Kasper, J. S. Complex alloy structures regarded as sphere packings. I. Definitions and basic principles. *Acta Crystallogr.* **1958**, *11*, 184–190.

(56) Sheng, H. W.; Luo, W. K.; Alamgir, F. M.; Bai, J. M.; Ma, E. Atomic packing and short-to-medium-range order in metallic glasses. *Nature* **2006**, *439*, 419–425.

(57) Kartouzian, A. Cluster-assembled metallic glasses. *Nanoscale Res. Lett.* **2013**, *8*, 1–4.

(58) Fan, C.; Liaw, P. K.; Liu, C. T. Atomistic model of amorphous materials. *Intermetallics* **2009**, *17*, 86–87.

(59) Fan, C.; Liaw, P. K.; Wilson, T. W.; Dmowski, W.; Choo, H.; Liu, C. T.; Richardson, J. W.; Proffen, T. Structural model for bulk amorphous alloys. *Appl. Phys. Lett.* **2006**, *89*, 111905-1–111905-3.

(60) Miracle, D. B. A structural model for metallic glasses. *Nat. Mater.* **2004**, *3*, 697–702.